Improved Thermosphere Mass Density Recovery During the 5 April 2010 Geomagnetic Storm by Assimilating NO Cooling Rates in a Coupled Thermosphere-Ionosphere Model

Jianhui He, Nicholas M. Pedatella, Elvira Astafyeva, Xinan Yue, Zhipeng Ren, Tingting Yu

JGR Space Physics

RESEARCH ARTICLE
10.1029/2023JA031959

Key Points:

- Assimilating nitric oxide cooling rate profiles into coupled thermosphere-ionosphere model results in improved thermosphere density recovery
- The improved density recovery is due to the impact of the assimilated observations on the general circulation and cooling processes
- Improved representation of cooling processes in the storm's main phase improves forecasts of the thermosphere mass density recovery

Supporting Information:

Supporting Information may be found in the online version of this article.

Correspondence to:

X. Yue,
yuexinan@mail.iggcas.ac.cn

Citation:

He, J., Pedatella, N. M., Astafyeva, E., Yue, X., Ren, Z., & Yu, T. (2023). Improved thermosphere mass density recovery during the 5 April 2010 geomagnetic storm by assimilating NO cooling rates in a coupled thermosphere-ionosphere model. *Journal of Geophysical Research: Space Physics*, *128*, e2023JA031959. https://doi.org/10.1029/2023JA031959

Received 1 AUG 2023
Accepted 26 OCT 2023

Improved Thermosphere Mass Density Recovery During the 5 April 2010 Geomagnetic Storm by Assimilating NO Cooling Rates in a Coupled Thermosphere-Ionosphere Model

Jianhui He[1,2,3], Nicholas M. Pedatella[4], Elvira Astafyeva[5], Xinan Yue[1,2,3], Zhipeng Ren[1,2,3], and Tingting Yu[1,2,3]

[1]Key Laboratory of Earth and Planetary Physics, Institute of Geology and Geophysics, Chinese Academy of Sciences, Beijing, China, [2]College of Earth and Planetary Sciences, University of Chinese Academy of Sciences, Beijing, China, [3]Beijing National Observatory of Space Environment, Institute of Geology and Geophysics, Chinese Academy of Sciences, Beijing, China, [4]High Altitude Observatory, National Center for Atmospheric Research, Boulder, CO, USA, [5]Université Paris Cité, Institut de Physique du Globe de Paris (IPGP), CNRS, Paris, France

Abstract The recovery of thermosphere mass density following geomagnetic storms is a result of competing heating and cooling processes. Simulations often underestimate the speed of the recovery. In this study, for the first time, we report that assimilating the Thermosphere Ionosphere Mesosphere Energetics and Dynamics Sounding of the Atmosphere using Broadband Emission Radiometry nitric oxide (NO) cooling rate profiles into a coupled thermosphere-ionosphere model via the ensemble Kalman filter improves the thermosphere mass density recovery following a geomagnetic storm. This is due to the impact of the assimilation on both the cooling processes and the thermosphere circulation. The dynamical changes due to the assimilation include stronger upwelling and equatorial transport. These lead to an effective increase in NO at all altitudes at mid-high latitudes, resulting in the improved recovery. The improved representation of cooling processes in the storm's main phase also results in improved >24 hr forecasts of the density recovery.

Plain Language Summary Since nitric oxide (NO) infrared emission plays the most important role in cooling down the thermosphere during storm times, it is plausible to attribute the slow neutral mass density recovery to an inaccurate representation of NO cooling in the simulations. In this study, for the first time, we assimilate the Thermosphere Ionosphere Mesosphere Energetics and Dynamics/Sounding of the Atmosphere using Broadband Emission Radiometry NO cooling rate profiles into a coupled thermosphere-ionosphere model. We found that the improved density recovery is obtained due to the impact of the assimilated observations on the general circulation and cooling processes. The improved representation of cooling processes in the storm's main phase further improves forecasts of the neutral density recovery.

1. Introduction

Nitric oxide (NO) is a minor constituent of Earth's lower thermosphere, where it plays an important role in the structure and energetics of the thermosphere. NO has a long chemical life time and a maximum near 110 km altitude. The distribution of NO density in the lower thermosphere is highly variable in space (i.e., latitude-longitude) and time. There are two principal energy sources that lead to the production of NO, both of which are highly variable, solar soft X-rays and auroral electron precipitation (Barth et al., 1999; Siskind et al., 1989). During storm time, the NO density increases significantly at higher latitudes, whereas the compressional heating, molecular diffusion and meridional transport from higher latitudes contribute to the variation in low latitudes (Barth & Bailey, 2004; Bharti et al., 2018; Dobbin et al., 2006). Infrared radiative cooling by NO at 5.3 μm measured by the Thermosphere Ionosphere Mesosphere Energetics and Dynamics (TIMED) Sounding of the Atmosphere using Broadband Emission Radiometry (SABER) instrument is a dominant cooling mechanism and influences the recovery of the thermosphere to geomagnetic storms (Hunt et al., 2011; Mlynczak et al., 2015). Lu et al. (2010) attribute this type of radiative cooling to the dissipation of nearly 80% of Joule heating and energy input during storm periods. Mlynczak et al. (2003) considered NO emission as an effective "thermostat" effect on the thermosphere.

Physics-based models, for example, the Thermosphere-Ionosphere-(Mesosphere)-Electrodynamics General Circulation Model (TI(M)EGCM), usually show a fairly good agreement with NO flux observations in terms

of Solar cycle variations, multiday oscillations, as well as daily global averages during storm times (Burns et al., 2012; Qian et al., 2010; Solomon et al., 2012). However, there remains a discrepancy between simulations and observations in terms of the neutral density recovery following geomagnetic storms. Lu et al. (2014) found the simulated density had a longer recovery time than the observations. Simulations also fail to reproduce thermospheric overcooling, where the thermosphere temperature and density decrease to below the pre-storm period following strong geomagnetic storms (Lei et al., 2012). One reason for these deficiencies may be an underestimation of the cooling processes for a particular storm case, that is, Knipp et al. (2013) showed many failed storm's density forecasts were associated with high levels of NO cooling. It should also be noted that the altitude distribution of the NO cooling rate differs significantly between simulations and observations. Li et al. (2018) found that the SABER peak cooling altitude usually exceeds that from TIEGCM, sometimes by as much as 16 km. This leads to an underestimation of the NO flux in TIEGCM due primarily to the lower cooling rates at 140–200 km in the model. The deficiencies in simulations of the thermosphere recovery suggest that the heating, circulation, and/or cooling processes are not adequately represented in the simulations, and also that updates to some parameterization schemes in the first-principle models are warranted.

Thermosphere-ionosphere data assimilations have been proven to obtain states that are more realistic than the numerical model simulations alone via the combination of both the experimental measurements and the state-of-the-art physical-based models (Chartier et al., 2016; Chen et al., 2017; Codrescu et al., 2018; Lee et al., 2012; Matsuo & Araujo-Pradere, 2011; Sutton, 2018). Most of the earlier thermosphere-ionosphere assimilation efforts were primarily restricted to the assimilation of ionosphere observations. They showed a positive impact on short-term forecasts and analyses (He et al., 2019; Hsu et al., 2014; Pedatella et al., 2020). This is due to the massive ionosphere-related measurements, such as the Global Navigation Satellite System and the Constellation Observing System for Meteorology, Ionosphere, and Climate. Recently, with the increased availability of thermosphere observations from the SABER, the Global-scale Observations of the Limb and Disk and the Ionospheric Connection Explorer) and the accelerometer-based one, they provide a unique opportunity for the joint thermosphere-ionosphere assimilation for the better forecast capability of the space weather.

In this study, for the first time, the SABER NO cooling rate profiles are assimilated into TIEGCM using an ensemble Kalman filtering (EnKF) to investigate the thermosphere recovery during the 5 April 2010 geomagnetic storm. This storm was driven by a fast-moving coronal mass ejection. Despite being a moderate storm with a minimum Dst near −50 nT, the event exhibited elevated thermospheric density more typically seen during major storms (Lu et al., 2014). The detailed space weather indices are provided in Figure S1 in Supporting Information S1. This storm was associated with a fast interplanetary coronal mass ejection traveling at a speed exceeding 700 km/s. It arrived at the Earth on 5 April and triggered a geomagnetic storm. The maximum Kp is closer to 8 at this moment. The interplanetary magnetic field (IMF) Bz components remained southward, and the geomagnetic symmetric disturbances for H components reached a minimum of ∼−90 nT on 6 April. Thereafter, the thermospheric recovery phase began on 7 April. The IMF returned to its pre-ICME condition in the following days and the Joule heating energy dissipation in the thermosphere subsided. Previous model-data comparisons by Lu et al. (2014) have already shown that the simulations overestimated the thermosphere recovery time. According to Kockarts (1980), the NO cooling rate is a derived quantity, given as a function of primary physical variables of NO, kinetic temperature, atomic oxygen and molecular oxygen. Therefore, the purpose of this study is to demonstrate and examine that applications of assimilating NO cooling rate to constraint these thermospheric parameters will lead to an improvement in heating, thermosphere dynamics, and cooling through self-consistent coupled thermosphere-ionosphere TIEGCM at each data assimilation cycle, which further contributes to a better specification and forecast of thermospheric neutral density recovery.

2. Data Assimilation Experiments Description

The EnKF data assimilation (DA) system built by He et al. (2019) was used in this study. The National Center for Atmospheric Research TIEGCM is chosen as the background model. In this study, we used the model version 2.0 with horizontal resolution of 2.5° × 2.5° in geographic latitude and longitude, and a vertical resolution of 1/4 scale height. The high latitude ion convention pattern is specified based on the Heelis empirical model, which is driven by the geomagnetic Kp index (Heelis et al., 1982). The solar UV and extreme ultraviolet fluxes are parameterized as the solar 10.7 cm radio flux (F10.7). The atmospheric migrating and non-migrating tides are specified at the model lower boundary by the Global Scale Wave Model (Hagan & Forbes, 2003). We use 60 ensemble members, and the ensemble simulations are initialized by perturbing solar F10.7 and Kp indices via centered Gaussian distributions.

The realistic F10.7 and Kp values used in this study are provided in Figure S1 in Supporting Information S1. Except for a storm as indicated above, the solar activity is under a lower condition with the solar 10.7 cm radio flux from 75 to 79 (unit: 10^{-22} W/m^2/Hz) during the whole data assimilation period. The time-dependent F10.7 and Kp indices from the gpi file are perturbed with a 15% standard deviation. We reset any F10.7 value less than 60 to 60 sfu. Similarly, Kp index values were restricted from 0 to 9. The background error covariance is localized by a Gaspari-Cohn function with a half-width of 20° and 40 km in the horizontal and vertical direction (Gaspari & Cohn, 1999).

The SABER NO cooling rate profiles are assimilated into TIEGCM hourly using observations within ±30 min. The assimilation period is from 01 to 09 April 2010. The NO cooling rate at 5.3 μm is calculated between 100 and 250 km by applying an Abel inversion for NO limb radiance profile. Meanwhile, a factor is applied to account for the width of the spectral band-pass of the filter in the SABER NO channel (Mlynczak et al., 2005, 2007). In details, the SABER instrument is a limb scanning radiometer that records vertical profiles of infrared emission from approximately 300 km tangent altitude down to the Earth's surface in 10 distinct channels from 1.27 to 15 μm. Infrared radiance profiles for NO at 5.3 μm are inverted to yield vertical profiles (~1,500 per day) of infrared cooling rates between 100 and 250 km at approximately 0.2 km altitude spacing. The NO cooling rate profiles are given as a function of altitude, geographic latitude and geographic longitude at tangent point. During the assimilation period, SABER was in southward viewing mode and sampled the thermosphere from ~83°S to ~55°N. The observation error is ~15%, which partially controls the weight assigned to an observation during data assimilation. Mlynczak et al. (2010) indicated that the observation errors include measurement errors, rotational temperature uncertainties, and improper filter function. They estimated the cooling rates due to NO to be accurate to better than 15%, that is, radiometric calibration (1%), rotational temperature uncertainties (~10%), and correcting for the spectral response filter function of the SABER NO channel (~10%). Assuming these uncertainties are uncorrelated, the root sum square of these is conservatively ~15%.

As discussed above, the modeled NO cooling rate is a computed quantity that depends on the state of the thermosphere. We therefore update the following unobserved model state variables in data assimilation: nitric oxide (NO), kinetic temperature (TN), atomic oxygen (O) and molecular oxygen (O_2). In the standard version of the TIEGCM, the NO cooling rate is calculated using relations derived by Kockarts (1980):

$$L_{\mathrm{NO}} = \frac{h\upsilon_0 A_{10} n(\mathrm{NO}_{v=0}) \times (K_O n(O) + K_{O2} n(O_2))}{K_O n(O) + K_{O2} n(O_2) + A_{10}} \times e^{-\frac{h\upsilon_0}{K_B T_N}} \quad (1)$$

where h, K_B, and T_N on the right-hand side are the Planck's constant, the Boltzmann's constant, and neutral temperature, respectively. The frequency $\upsilon_0 = \frac{C}{\lambda_0}$, where C is the speed of light, $\lambda_0 = 5.3$ μm. A_{10} is the Einstein coefficient of transition of NO from vibrational level $v = 1$ to $v = 0$; $n(\mathrm{NO}_{v=0})$, $n(O)$, and $n(O_2)$ are number densities of NO, atomic oxygen and molecular oxygen, respectively. K_O is the vibrational relaxation rate of NO by collisions with O. K_{O2} is the vibrational relaxation rate of NO by collisions with O_2. According to the above equation, the NO cooling rate depends primarily on three factors: temperature, atomic oxygen density, and NO density. The temperature-dependent collision of O_2 with N(^{2}D, ^{4}S) always acts as a dominant source for the production of NO during auroral and geomagnetic activity (Barth, 1992). This temperature-dependent reaction rate coefficient is responsible for the difference in the peak altitude of NO density (~105 km) and NO cooling rate (~120–130 km). However, for the NO production around its peaked altitude, the reaction rate of N(^{2}D) + O_2 in the TIEGCM is a constant coefficient. This would cause a negative performance for the NO emission specification during storm time. Previously, Duff et al. (2003) suggested that a linear temperature-dependent reaction rate should be considered.

We performed three different experiments to assess the impact of assimilating the SABER NO cooling rate. A TIEGCM run (hereafter DA) with assimilation during the days from 01 to 09 April. We refer to the prior 1 hr forecast as "DA/Prior," and the analysis as "DA/Posterior." We additionally performed a TIEGCM default run without assimilation (hereafter control) that is driven by the realistic F10.7 and Kp values. Last, we performed a TIEGCM forecast run (hereafter forecast) with assimilation from 01 to 06 April, at which point the model is run without any further data assimilation the rest of the time period (i.e., 07–09 April). The purpose of the forecast experiment is to examine the extent to which the improved heating, dynamics, and cooling processes during the data assimilation period result in a better forecast of thermospheric neutral density recovery.

3. Results and Discussion

Figure 1 displays the TIMED/SABER observational coverage (a) and the difference between DA/Prior and control around the peak NO emission altitude (ZP = −3.875, ~120 km) for thermosphere parameters (i.e., TN, NO, and

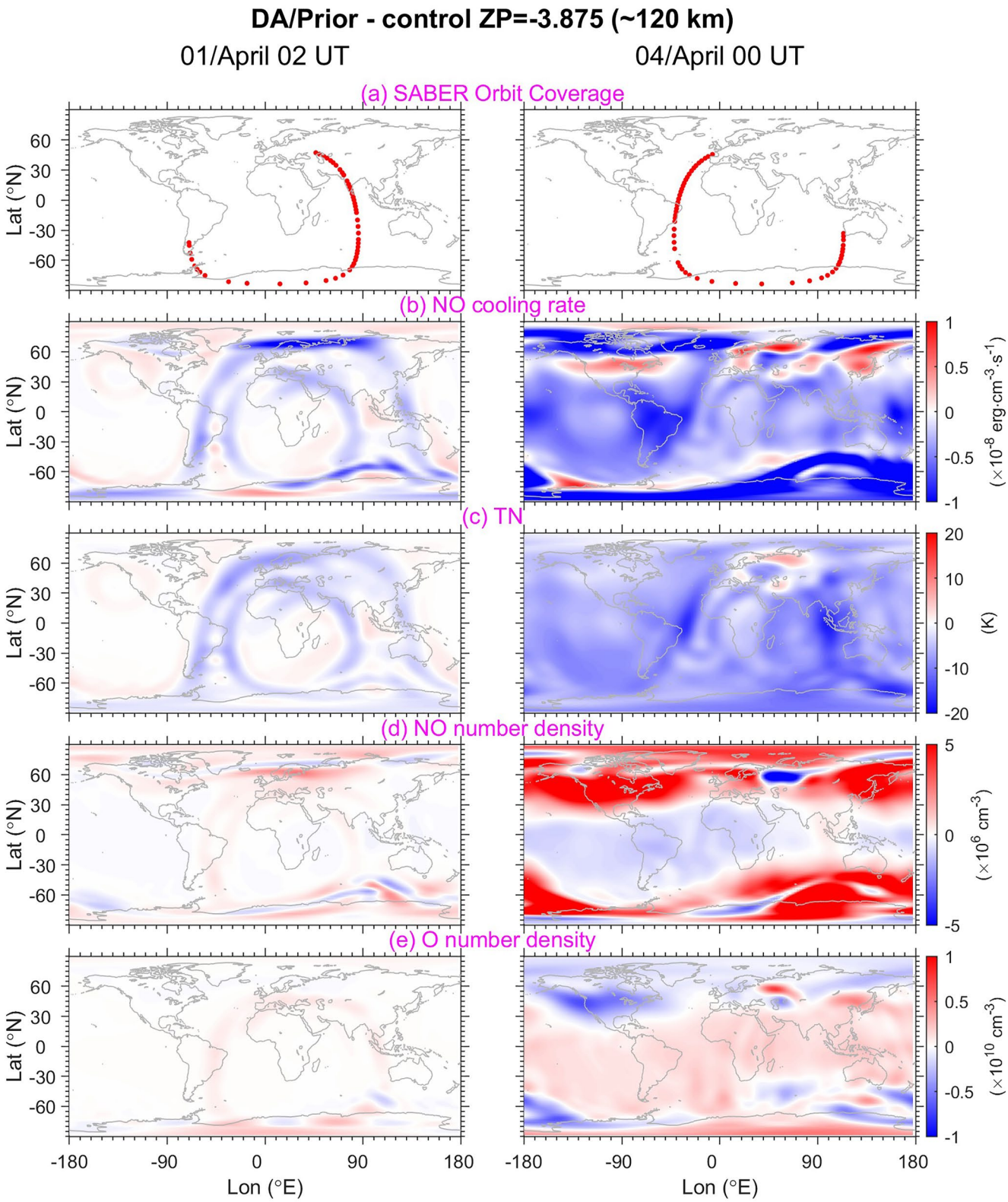

Figure 1. The (a) Sounding of the Atmosphere using Broadband Emission Radiometry observational coverage, and the difference between DA/Prior and control for (b) nitric oxide (NO) cooling rate, (c) TN, (d) NO and (e) O number density around the peak NO emission altitude (ZP = −3.875, ~120 km) at 02 UT on 01 April (the left panels) and 00 UT on 04 April (the right panels), respectively.

O) (c–e) that influence the NO cooling rate (b). Note that "ZP" indicates the pressure level used in TIEGCM. The results in Figure 1 illustrate the impact of assimilating the NO cooling rate observations on global thermosphere parameters. At the second assimilation epoch, that is, 02 UT on 01 April (left panels), the thermosphere states are only adjusted around the locations of the observations. However, with time these states are adjusted globally, and relatively global influence is evident after several assimilation cycles, that is, 00 UT on 04 April (right panels). The results thus demonstrate that assimilating sparse SABER NO cooling rate observations can have a global impact on the state of the thermosphere.

Figure 1 shows that there is a negative difference between DA/Prior and control in NO cooling rate, which means that the control overestimated the cooling rates in the lower thermosphere. This is consistent with Li et al. (2018). They found the maximum NO cooling rate derived from the TIEGCM is larger than that from SABER due to a model temperature overestimation caused by the effects of tides at the model lower boundary. They also found lower cooling rates at ∼140–200 km in the TIEGCM. Figure S2 in Supporting Information S1, which is the same as Figure 2 but for higher in the thermosphere (ZP = −0.125, ∼200 km), also supports their conclusion.

Figure 1 also illustrates that how the assimilation of NO cooling rate observations impacts the TN, NO, and O number densities. We found the variations in temperature are similar to the NO cooling rate, that is, larger temperature in upper thermosphere and smaller one in lower thermosphere. The anti-correlation between NO and O number density occurred on a global scale. In particular, at mid-high latitudes there is an increase in NO density and decrease in O density, and vice versa in lower latitudes. This could be due to the fact that the changed TN results in the upwelling of nitrogen-rich/oxygen-poor air from lower to higher altitudes. The increases in O_2 and TN are in turn responsible for the increased NO production. This is similar to an anti-correlated feature between storm time O/N_2 depletion and NO density (Zhang et al., 2014).

To investigate the improvement in NO cooling rates in TIEGCM, Figure 2 shows the root-mean-square error (RMSE) of the NO cooling rate for the control, DA/Prior and DA/Posterior during the whole data assimilation period. The RMSE is calculated relative to the NO cooling rate observations. For the control, the largest RMSEs occur around the altitude range of 110–130 km relative to other heights. Compared to the quiet days (01–04 April), there are increased RMSEs during the geomagnetic storm period (e.g., 05–09 April). As expected, the RMSE smaller in the DA/Prior and DA/Posterior cases compared to the control, indicating effective assimilation of the NO cooling rate observations. Quantitatively, from Figure 2b, the average RMSEs in the whole altitude range and for the whole data assimilation period are 1.2×10^{-8} (unit: erg/cm^3/s) for the control, 1.0×10^{-8} for DA/Prior, and 0.9×10^{-8} for DA/Posterior. Around the peak NO cooling rate altitude (110–130 km, Figure 2c), the RMSEs for the control are 5.1×10^{-8}, and 4.3×10^{-8} and 3.6×10^{-8} for DA/Prior and DA/Posterior, respectively. Thus, we confirm an improved representation of the NO cooling in the TIEGCM run with the assimilation, which can be up to ∼15% for DA/Prior, and ∼30% for DA/Posterior during the whole data assimilation period. Due to the background error covariance, which is estimated from the ensemble members at each assimilation cycle, the assimilated cooling rate may be weakly correlated with some of the chosen thermosphere state vectors (e.g., NO, O, and O_2). A weak constraint for minimized cost function would happen for the assimilation analysis. Thus, even though the NO cooling rate is assimilated, the improvement of DA/Posterior may be limited.

To investigate how the NO cooling-rate-related thermosphere states change, Figure 3a further shows the global mean TN, O_2 and O number density comparison between the control and DA/Prior. Relative to the control, TN is increased evidently in DA/Prior due to the assimilation of the larger NO cooling rate in middle thermosphere as discussed previously. The DA/Prior also exhibits larger O_2 and smaller O number densities compared to the control. This implies stronger upwelling effects in DA/Prior. To illustrate this, Figure 3b shows the integrated O/N_2 (hereafter $[O/N_2]$) for Global Ultraviolet Imager (GUVI) observations, control and DA/Prior at a fixed local time (LT) of ∼7.5 during the days from 04 to 09 on April. The GUVI $[O/N_2]$ shows an obvious depletion at higher latitudes, and an evident equatorward transport during the storm's main phase (e.g., 05–06 April). The $[O/N_2]$ depletion is still present during the recovery phase, that is, 07–09 April. For the control case, there exists a weaker $[O/N_2]$ depletion in middle and high latitudes of both northern and southern hemispheres throughout the whole data assimilation period. However, these features have been adjusted in DA/Prior, which are more consistent with the observations especially at higher latitudes. Quantitatively, the difference between control and GUVI $[O/N_2]$ is −0.19 in middle and high latitudes of both northern and southern hemispheres, and −0.06 in low latitudes. However, the differences for DA/Prior results are −0.06 and −0.03, respectively. Physically, storm-induced heating would cause the thermosphere circulation changes, and further neutral compositions variations. The upward winds could transport the oxygen-poor/nitrogen-rich air to higher altitudes, resulting in polar $[O/N_2]$ depletion. The meridional wind transports the polar depleted air to

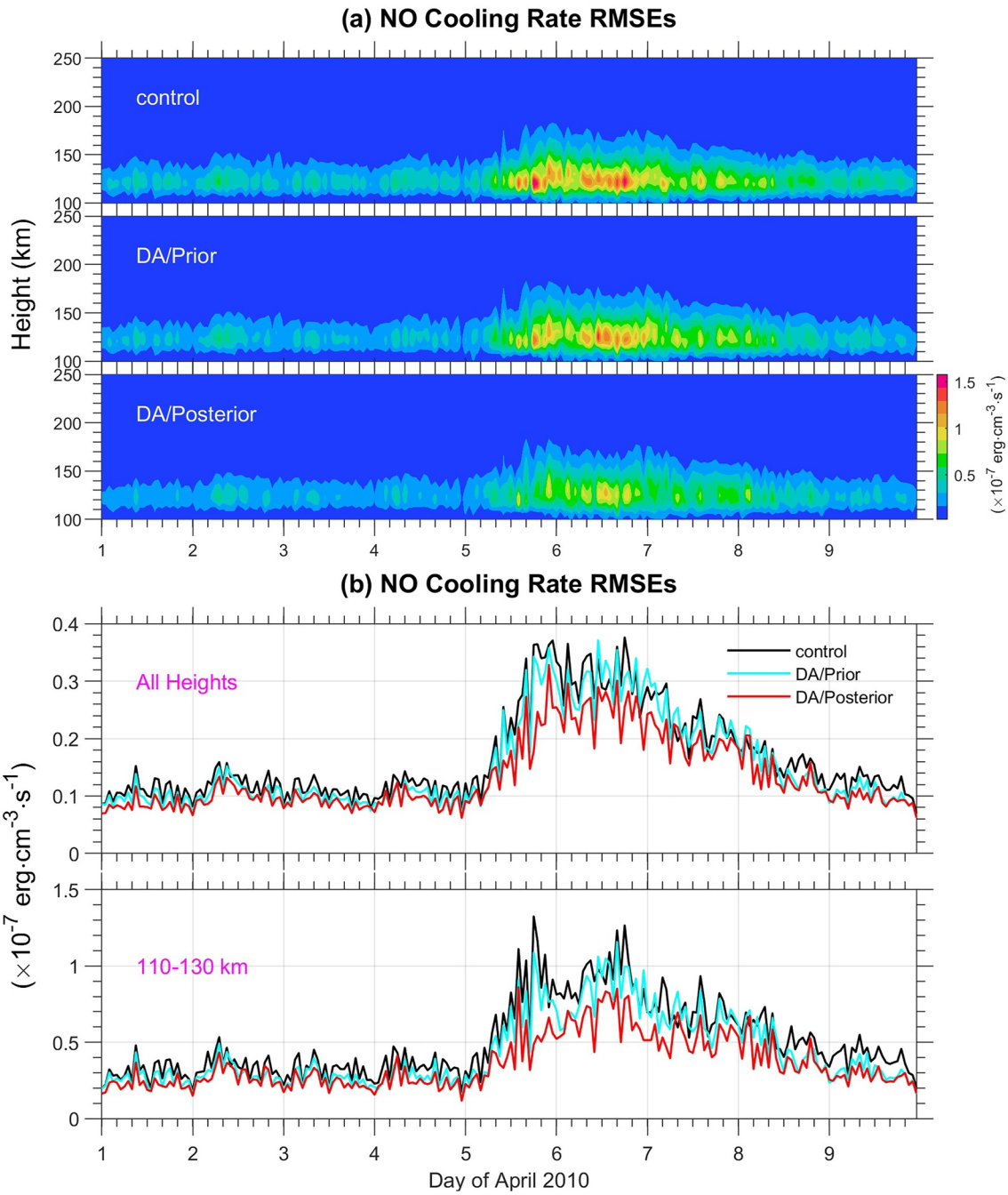

Figure 2. (a) The nitric oxide cooling rate RMSEs of the control, DA/Prior and DA/Posterior in comparison with the Sounding of the Atmosphere using Broadband Emission Radiometry observations in the altitude range of 100–250 km during the whole data assimilation period. (b) The root-mean-square errors comparison in the whole altitude range and around 110–130 km. The black, cyan, and red lines denote control, DA/Prior and DA/Posterior, respectively.

mid-latitudes, or even to low-latitudes (Prolss et al., 1975). The more consistent [O/N_2] changes in DA/Prior indicate a stronger and better adjustment of the general circulation, that is, the stronger upwelling and equatorward transport.

As indicated above, the enhanced neutral temperature and collision of molecular oxygen with N(^{2}D, ^{4}S) act as a dominant source for the production of NO during auroral and geomagnetic activity (Barth, 1992). In TIEGCM, a temperature-dependent reaction rate is used in the reaction of N(^{4}S) + O_2 for NO density production above 150 km. However, a constant reaction coefficient is applied for the loss of N(^{2}D) reacting with O_2, which is the primary source of NO at its peak altitude (~110 km). As shown in Figure 4a, the DA/Prior has increased global

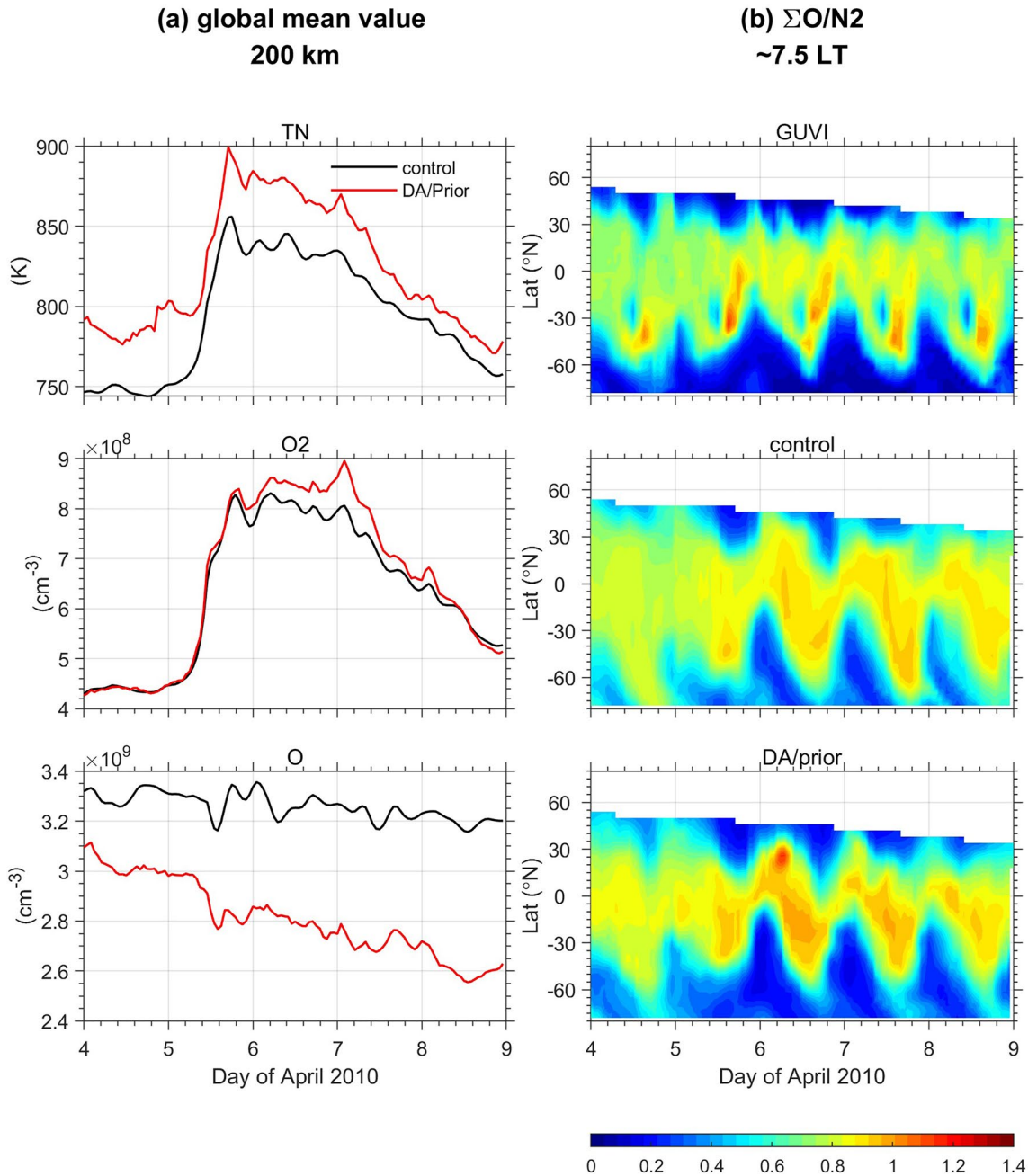

Figure 3. (a) Time series of the global mean TN, the number density of O_2 and O comparison among control and DA/Prior during the days from 04 to 09 April. (a) The latitudinal-universal time distribution of the integrated O/N_2 comparison among Global Ultraviolet Imager observations, control and DA/Prior at a fixed local time (LT) (~7.5 LT) during the days from 04 to 09 April.

mean NO number density compared to the control above 150 km. This is expected due to the enhancements in O_2 number density and neutral temperature in DA/Prior. However, there exists an increased NO density at 110 km. Richards (2004) suggested that vertical diffusion is a net sink of NO at 150 km but an important source at 110 km.

To investigate the main reason for the NO density changes, we give the diagnostic analysis of the physical processes of the storm-time changes in NO for the control case during the daytime, including the chemical term (i.e., production and loss), transport term (i.e., horizontal and vertical advection) and molecular and eddy diffusion. In TIEGCM, the continuity equation of Ψ_{NO} on a constant pressure surface is expressed as (Roble et al., 1988)

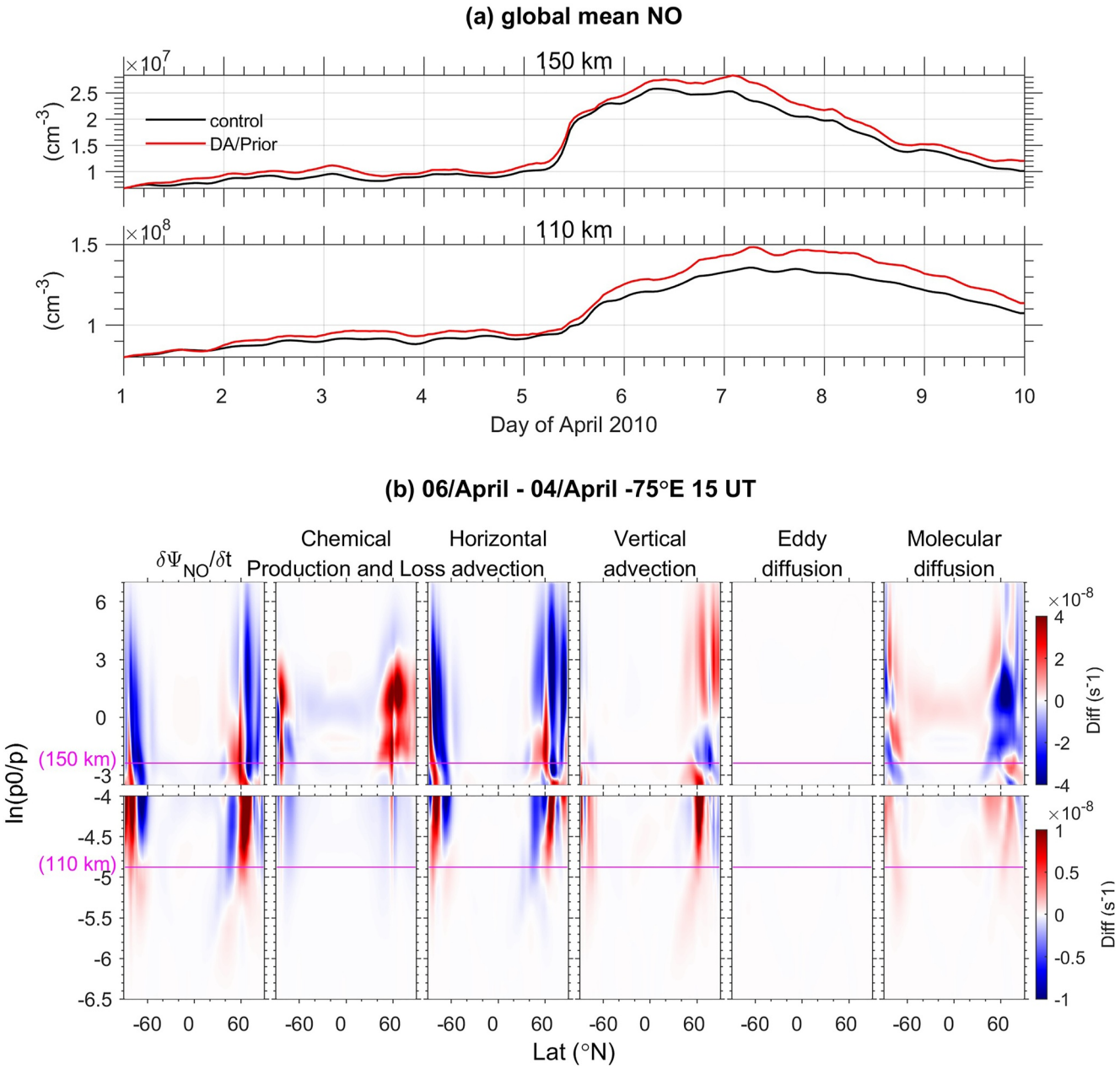

Figure 4. (a) Time series of the global mean nitric oxide (NO) number density at 110 and 150 km for control and DA/Prior during the whole data assimilation period. (b) Latitude-pressure surface distributions of the storm-quiet differences in NO rate of change, chemical production-loss, horizontal advection, vertical advection, eddy diffusion, and molecular diffusion for the control case at the longitude of −75°W at 15 UT (10 local time). The magenta solid lines of top and bottom panels denote 150 and 110 km. Note that these two panels have different color bars to show the perturbation structures of these parameters clearly.

$$\frac{\partial \Psi_{\mathrm{NO}}}{\partial \mathrm{t}} = -e^{z}\frac{\partial\left[A\left(\frac{\partial}{\partial z}-E\right)\Psi_{\mathrm{NO}}\right]}{\partial z} + S\Psi_{\mathrm{NO}} - R - \left[\mathrm{V}_n\cdot\nabla\Psi_{\mathrm{NO}} + W_n\frac{\partial\Psi_{\mathrm{NO}}}{\partial \mathrm{z}}\right] + e^{z}\frac{\partial\left[e^{-z}K_E\left(\frac{\partial}{\partial z}+\frac{1}{\overline{m}}\frac{\partial\overline{m}}{\partial z}\right)\Psi_{\mathrm{NO}}\right]}{\partial z} \quad (2)$$

where the vertical coordinates $z = \ln(P_0/P)$, where P_0 is the reference pressure and P is the pressure. The vertical molecular diffusion coefficient is A. The term E includes the effects of gravity, thermal diffusion and friction with the major species on the vertical profile of the two species. K_E is the eddy diffusion coefficient. $\overline{m}$ is the mean molecular mass of the air. S and R represent the chemistry production and loss rate. V_n is the horizontal wind velocity along a constant pressure surface, and W_n is the "vertical tendency," or vertical wind velocity divided by

the scale height. The terms on the right-hand side of the equation are: molecular diffusion ($-e^z \frac{\partial\left[A\left(\frac{\partial}{\partial z}-E\right)\Psi_{NO}\right]}{\partial z}$), eddy diffusion ($e^z \frac{\partial\left[e^{-z}K_E\left(\frac{\partial}{\partial z}+\frac{1}{m}\frac{\partial m}{\partial z}\right)\Psi_{NO}\right]}{\partial z}$), horizontal advection ($V_n \cdot \nabla\Psi_{NO}$), vertical advection ($W_n \frac{\partial\Psi_{NO}}{\partial z}$) and chemical term ($S\Psi_{NO} - R$). Comparing the magnitude and distribution of $\frac{\partial\Psi_{NO}}{\partial t}$ and each term on the right-hand side, we can determine the relative contributions of the main physical processes to the simulated storm-time composition variations.

The NO variations are mainly confined to the middle and high latitudes at this time (Figure 4b, left panels). From Figure 4b, it is evident that the NO variations are height dependent. Above 150 km, the changes in NO were influenced by all terms except for the eddy diffusion. There exists a large contribution from the chemical term; however, these changes are balanced out by changes in molecular diffusion. The horizontal and vertical advections dominate the NO changes. Around 110 km, the transport processes and molecular diffusion dominate the changes in NO, and the effects of the former are greater than that of the latter. Overall, the transport processes, including the horizontal and vertical advection, still play an important role in the changes in NO at both 110 km and above 150 km. The same conclusion can also be obtained for DA/Prior in Figure S3 in Supporting Information S1. Meanwhile, due to stronger circulation dynamics in DA/prior as indicated above, we found a larger change of all terms of NO in the whole range of heights, especially for the advection terms. During a geomagnetic storm, the meridional winds transport energy and NO-enhanced air from high latitudes to middle and low latitudes near 150 km, which in turn diffuse and advect downward to ∼110 km. These combined effects could lead to more NO density on global scale in DA/Prior as shown in Figure 4a.

The NO created at high latitudes during geomagnetic storms can spread out to lower latitudes due to its long lifetime. Since NO radiation is an important sink of thermospheric energy, the middle latitude source is likely to be important in speeding the recovery of the thermosphere following geomagnetic storms (Knipp et al., 2017; Lei et al., 2011; Mlynczak et al., 2018; Zesta & Oliveira, 2019). Figure 5 shows the thermosphere mass density comparison among observations, control, DA/Prior and forecast at different heights and local times. Three different density data sets at different altitudes are considered: GRACE (∼474.7 km), CHAMP (∼300.4 km), and GOCE (∼270 km). We found that there exists an obvious neutral density difference between simulations and observations at different altitudes. The thermosphere mass density response with altitude is strongly impacted by composition change during geomagnetic activity period. The altitude distribution of these major species is basically represented by diffusive equilibrium by their respective molecular weights. The altitude where these transitions occur is temperature dependent through their individual scale heights (Burns et al., 2006, 2007; Thayer et al., 2012). Therefore, the manner in which composition transitions with height will impact the mass density response difference between observations and simulations.

For the higher altitude GRACE measurements, the neutral mass density shows a larger value for DA/Prior than control at different local times during the storm's main phase, that is, 05–06 April. Then, the values of both DA/Prior and control are comparable, and close to the observations during the storm's recovery phase (shadow area). This is due to a faster thermosphere density recovery in DA/Prior compared to the control. Compared to control, the DA/Prior is in better agreement with the observations that occurred at lower altitudes (i.e., CHAMP and GOCE) during the recovery phase. In addition, the neutral temperature, the mean molecular mass and NO cooling rate along each satellite orbit are also shown in Figures S4–S6 in Supporting Information S1. The quick decrease in neutral temperature caused by enhanced NO emission, and the heavier molecules transported by the upward winds, reduce the scale height and thus reduce the neutral density at satellite altitudes (Chen & Lei, 2018; Lei et al., 2010).

To further demonstrate how the improved cooling processes during the storm's main phase contribute to a better forecast of thermospheric mass density recovery, Figure 5 also shows the forecast results (green lines). It is evident that the density recovery in the forecast case closely follows the DA/Prior case on 07 April. The thermosphere density recovery in the forecast experiments is weaker than that of the DA/Prior during the days of 08–09 April, which is due to the fact that the cooling processes are still adjusted for each data assimilation epoch in the DA/Prior case, but it is no longer being adjusted in the forecast case. However, the thermosphere mass density recovery in the forecast case is still better than the control case. Overall, this demonstrates that the improved cooling processes in the storm's main phase could contribute to a >24 hr forecast of thermospheric neutral density recovery.

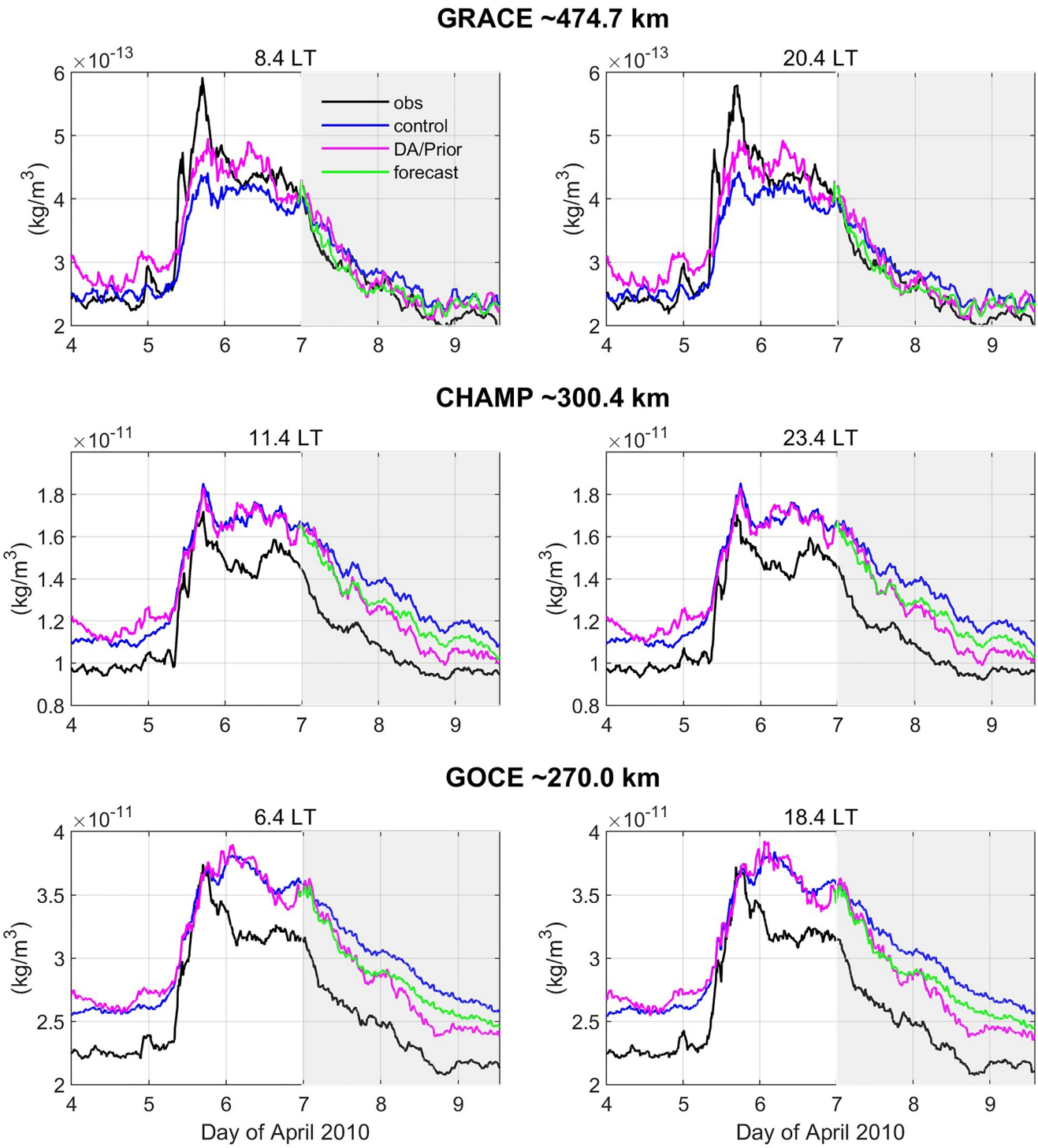

Figure 5. The time series of the thermosphere mass density comparison among observations, control, DA/Prior and forecast at 474.7 km (GRACE), 300.4 km (CHAMP), and 270.0 km (GOCE) during the daytime (the left panels) and nighttime (the right panels) from 04 to 09 on April. The black, blue, magenta and green lines indicate observations, control, DA/Prior and forecast, respectively. The shadow area indicates the storm's recovery phase.

4. Summary

In this work, for the first time, the SABER NO cooling rate profiles are assimilated into TIEGCM to investigate the thermosphere mass density recovery during the 5 April 2010 geomagnetic storm. The main results of this

study are the following:

1. Assimilating sparse NO cooling rate observations has a positive impact on global cooling processes and improves the general circulation.
2. The stronger upwelling and equatorial transport contribute to the NO increase in all altitudes at mid-high latitudes, which result in a better thermosphere mass density recovery.
3. The improved cooling processes in the storm's main phase further contribute to a >24 hr forecast of thermosphere mass density recovery.

We note that the impact of assimilating NO cooling rate observations may be limited due to the sparse SABER observational coverage and only observing two local times per day. The NO cooling rate varies rapidly during storm times with notable hemispheric, spatial, and LT variabilities. Multiple satellite observations of NO cooling (e.g., Mlynczak et al., 2018) that resolve the spatial-temporal variabilities would likely improve the impact of observations on thermosphere neutral density. Detailed Observing System Simulation Experiments are necessary to understand how assimilation of additional NO cooling rate observations would impact the thermosphere neutral density specification and forecasting in the future.

Data Availability Statement

The thermosphere mass density data set can be downloaded from the ESA's Swarm website (swarm-diss.eo.esa.int). The TIMED/SABER NO emission data set are from GATS Data Server (saber.gats-inc.com). The simulation results are available at Open Science Framework (He et al., 2023).

Acknowledgments
This work was supported by the Project of Stable Support for Youth Team in Basic Research Field, CAS (YSBR-018), the National Natural Science Foundation of China (42104160), and the China Scholarship Council (CSC). This research was supported by the International Space Science Institute (ISSI) in Bern, through ISSI International Team project #537 Data Assimilation in the Ionosphere and thermosphere. We thank that Jiuhou Lei gave the valuable discussion on this manuscript.

References

Barth, C. A. (1992). Nitric oxide in lower thermosphere. *Planetary and Space Science*, *40*(2/3), 315–336. https://doi.org/10.1016/0032-0633(92)90067-x

Barth, C. A., Bailey, S. C., & Solomon, S. C. (1999). Solar-terrestrial coupling: Solar soft x-rays and thermospheric nitric oxide. *Geophysical Research Letters*, *26*(9), 1251–1254. https://doi.org/10.1029/1999gl900237

Barth, C. A., & Bailey, S. M. (2004). Comparison of a thermospheric photochemical model with Student Nitric Oxide Explorer (SNOE) observations of nitric oxide. *Journal of Geophysical Research*, *109*(A3), A03304. https://doi.org/10.1029/2003JA010227

Bharti, G., Sunil Krishna, M. V., Bag, T., & Jain, P. (2018). Storm time variation of radiative cooling by nitric oxide as observed by TIMED-SABER and GUVI. *Journal of Geophysical Research: Space Physics*, *123*(2), 1500–1514. https://doi.org/10.1002/2017JA024576

Burns, A., Solomon, S., Wang, W., & Killeen, T. (2007). The ionospheric and thermospheric response to CMEs: Challenges and successes. *Journal of Atmospheric and Solar-Terrestrial Physics*, *69*(1), 77–85. https://doi.org/10.1016/j.jastp.2006.06.010

Burns, A., Wang, W., Killeen, T., Solomon, S., & Wiltberger, M. (2006). Vertical variations in the N_2 mass mixing ratio during a thermospheric storm that have been simulated using a coupled magnetosphere-ionosphere-thermosphere model. *Journal of Geophysical Research*, *111*(A11), A11309. https://doi.org/10.1029/2006JA011746

Burns, A. G., Solomon, S. C., Qian, L., Wang, W., Emery, B. A., Wiltberger, M., & Weimer, D. R. (2012). The effects of corotating interaction region/high speed stream storms on the thermosphere and ionosphere during the last solar minimum. *Journal of Atmospheric and Solar-Terrestrial Physics*, *83*, 79–87. https://doi.org/10.1016/j.jastp.2012.02.006

Chartier, A. T., Matsuo, T., Anderson, J. L., Collins, N., Hoar, T. J., Lu, G., et al. (2016). Ionospheric data assimilation and forecasting during storms. *Journal of Geophysical Research: Space Physics*, *121*(1), 764–778. https://doi.org/10.1002/2014ja020799

Chen, C.-H., Lin, C., Chen, W.-H., & Matsuo, T. (2017). Modeling the ionospheric prereversal enhancement by using coupled thermosphere-ionosphere data assimilation. *Geophysical Research Letters*, *44*(4), 1652–1659. https://doi.org/10.1002/2016gl071812

Chen, X., & Lei, J. (2018). A numerical study of the thermospheric overcooling during the recovery phases of the October 2003 storms. *Journal of Geophysical Research: Space Physics*, *123*(7), 5704–5716. https://doi.org/10.1029/2017JA025120

Codrescu, S. M., Codrescu, M. V., & Fedrizzi, M. (2018). An ensemble Kalman filter for the thermosphere-ionosphere. *Space Weather*, *16*(1), 57–68. https://doi.org/10.1002/2017sw001752

Dobbin, A. L., Aylward, A. D., & Harris, M. J. (2006). Three-dimensional GCM modeling of nitric oxide in the lower thermosphere. *Journal of Geophysical Research*, *111*(A7), A07314. https://doi.org/10.1029/2005JA011543

Duff, J. W., Dothe, H., & Sharma, R. D. (2003). On the rate coefficient of the $N(^2D)+O_2 \rightarrow NO+O$ reaction in the terrestrial thermosphere. *Geophysical Research Letters*, *30*(5), 1259. https://doi.org/10.1029/2002GL016720

Gaspari, G., & Cohn, S. E. (1999). Construction of correlation functions in two and three dimensions. *Quarterly Journal of the Royal Meteorological Society*, *125*(554), 723–757. https://doi.org/10.1002/qj.49712555417

Hagan, M. E., & Forbes, J. M. (2003). Migrating and nonmigrating semidiurnal tides in the upper atmosphere excited by tropospheric latent heat release. *Journal of Geophysical Research*, *108*(A2), 1062. https://doi.org/10.1029/2002JA009466

He, J., Pedatella, N. M., Astafyeva, E., Yue, X., Ren, Z., & Yu, T. (2023). Improved thermosphere mass density recovery during the 5 April 2010 geomagnetic storm by assimilating NO cooling rates in a coupled thermosphere-ionosphere model [Dataset]. OSF. http://doi.org/10.17605/OSF.IO/KNY8X

He, J., Yue, X., Wang, W., & Wan, W. (2019). EnKF ionosphere and thermosphere data assimilation algorithm through a sparse matrix method. *Journal of Geophysical Research: Space Physics*, *124*(8), 7356–7365. https://doi.org/10.1029/2019JA026554

Heelis, R. A., Lowell, J. K., & Spiro, R. W. (1982). A model of the high-latitude ionospheric convection pattern. *Journal of Geophysical Research*, *87*(A8), 6339–6345. https://doi.org/10.1029/JA087iA08p06339

Hsu, C.-T., Matsuo, T., Wang, W., & Liu, J.-Y. (2014). Effects of inferring unobserved thermospheric and ionospheric state variables by using an ensemble Kalman filter on global ionospheric specification and forecasting. *Journal of Geophysical Research: Space Physics*, *119*(11), 9256–9267. https://doi.org/10.1002/2014JA020390

Hunt, L. A., Mlynczak, M. G., Marshall, B. T., Mertens, C. J., Mast, J. C., Thompson, R. E., et al. (2011). Infrared radiation in the thermosphere at the onset of solar cycle 24. *Geophysical Research Letters*, *38*(15), L15802. https://doi.org/10.1029/2011GL048061

Knipp, D., Kilcommons, L., Hunt, L., Mlynczak, M., Pilipenko, V., Bowman, B., et al. (2013). Thermospheric damping response to sheath-enhanced geospace storms. *Geophysical Research Letters*, *40*(7), 1263–1267. https://doi.org/10.1002/grl.50197

Knipp, D. J., Pette, D. V., Kilcommons, L. M., Isaacs, T. L., Cruz, A. A., Mlynczak, M. G., et al. (2017). Thermospheric nitric oxide response to shock-led storms. *Space Weather*, *15*(2), 325–342. https://doi.org/10.1002/2016SW001567

Kockarts, G. (1980). Nitric oxide cooling in the terrestrial thermosphere. *Geophysical Research Letters*, *7*(2), 137–140. https://doi.org/10.1029/GL007i002p00137

Lee, I. T., Matsuo, T., Richmond, A. D., Liu, J. Y., Wang, W., Lin, C. H., et al. (2012). Assimilation of FORMOSAT-3/COSMIC electron density profiles into a coupled thermosphere/ionosphere model using ensemble kalman filtering. *Journal of Geophysical Research*, *117*(A10), A10318. https://doi.org/10.1029/2012ja017700

Lei, J., Burns, A. G., Thayer, J. P., Wang, W., Mlynczak, M. G., Hunt, L. A., et al. (2012). Overcooling in the upper thermosphere during the recovery phase of the 2003 October storms. *Journal of Geophysical Research*, *117*(A3), A03314. https://doi.org/10.1029/2011JA016994

Lei, J., Thayer, J. P., Burns, A. G., Lu, G., & Deng, Y. (2010). Wind and temperature effects on thermosphere mass density response to the November 2004 geomagnetic storm. *Journal of Geophysical Research*, *115*(A5), A05303. https://doi.org/10.1029/2009JA014754

Lei, J., Thayer, J. P., Lu, G., Burns, A. G., Wang, W., Sutton, E. K., & Emery, B. A. (2011). Rapid recovery of thermosphere density during the October 2003 geomagnetic storms. *Journal of Geophysical Research*, *116*(A3), A03306. https://doi.org/10.1029/2010JA016164

Li, Z., Knipp, D., Wang, W., Sheng, C., Qian, L., & Flynn, S. (2018). A comparison study of NO cooling between TIMED/SABER measurements and TIEGCM simulations. *Journal of Geophysical Research: Space Physics*, *123*(10), 8714–8729. https://doi.org/10.1029/2018JA025831

Lu, G., Hagan, M. E., Häusler, K., Doornbos, E., Bruinsma, S., Anderson, B. J., & Korth, H. (2014). Global ionospheric and thermospheric response to the 5 April 2010 geomagnetic storm: An integrated data-model investigation. *Journal of Geophysical Research: Space Physics*, *119*(12), 10358–10375. https://doi.org/10.1002/2014JA020555

Lu, G., Mlynczak, M. G., Hunt, L. A., Woods, T. N., & Roble, R. G. (2010). On the relationship of Joule heating and nitric oxide radiative cooling in the thermosphere. *Journal of Geophysical Research*, *115*(A5), A05306. https://doi.org/10.1029/2009JA014662

Matsuo, T., & Araujo-Pradere, E. A. (2011). Role of thermosphere-ionosphere coupling in a global ionospheric specification. *Radio Science*, *46*(6), RS0D23. https://doi.org/10.1029/2010RS004576

Mlynczak, M., Javier Martin-Torres, F., Russell, J., Beaumont, K., Jacobson, S., Kozyra, J., et al. (2003). The natural thermostat of nitric oxide emission at 5.3 μm in the thermosphere observed during the solar storms of April 2002. *Geophysical Research Letters*, *30*(21), 2100. https://doi.org/10.1029/2003GL017693

Mlynczak, M. G., Hunt, L. A., Marshall, B. T., Russell, J. M., III, Mertens, C. J., Thompson, R. E., & Gordley, L. L. (2015). A combined solar and geomagnetic index for thermospheric climate. *Geophysical Research Letters*, *42*(10), 3677–3682. https://doi.org/10.1002/2015GL064038

Mlynczak, M. G., Hunt, L. A., Thomas Marshall, B., Martin-Torres, F. J., Mertens, C. J., Russell, J. M., et al. (2010). Observations of infrared radiative cooling in the thermosphere on daily to multiyear timescales from the TIMED/SABER instrument. *Journal of Geophysical Research*, *115*(A3), A03309. https://doi.org/10.1029/2009ja014713

Mlynczak, M. G., Knipp, D. J., Hunt, L. A., Gaebler, J., Matsuo, T., Kilcommons, L. M., & Young, C. L. (2018). Space-based sentinels for measurement of infrared cooling in the thermosphere for space weather nowcasting and forecasting. *Space Weather*, *16*(4), 363–375. https://doi.org/10.1002/2017SW001757

Mlynczak, M. G., Martin-Torres, F. J., Crowley, G., Kratz, D. P., Funke, B., Lu, G., et al. (2005). Energy transport in the thermosphere during the solar storms of April 2002. *Journal of Geophysical Research*, *110*(A12), A12S25. https://doi.org/10.1029/2005JA011141

Mlynczak, M. G., Martin-Torres, F. J., & Russell, J. M. (2007). Correction to "Energy transport in the thermosphere during the solar storms of April 2002". *Journal of Geophysical Research*, *112*(A2), A02303. https://doi.org/10.1029/2006JA012008

Pedatella, N. M., Anderson, J. L., Chen, C. H., Raeder, K., Liu, J., Liu, H.-L., & Lin, C. H. (2020). Assimilation of ionosphere observations in the whole atmosphere community climate model with thermosphere-ionosphere eXtension (WACCMX). *Journal of Geophysical Research: Space Physics*, *125*(9), e2020JA028251. https://doi.org/10.1029/2020ja028251

Prolss, G. W., Von Zahn, U., & Raitt, W. J. (1975). Neutral atmospheric composition, plasma density, and electron temperature at F region heights. *Journal of Geophysical Research*, *80*(25), 3715–3718. https://doi.org/10.1029/ja080i025p03715

Qian, L., Solomon, S. C., & Mlynczak, M. G. (2010). Model simulation of thermospheric response to recurrent geomagnetic forcing. *Journal of Geophysical Research*, *115*(A10), A10301. https://doi.org/10.1029/2010JA015309

Richards, P. G. (2004). On the increases in nitric oxide density at midlatitudes during ionospheric storms. *Journal of Geophysical Research*, *109*(A6), A06304. https://doi.org/10.1029/2003JA010110

Roble, R. G., Ridley, E. C., Richmond, A. D., & Dickinson, R. E. (1988). A coupled thermosphere/ionosphere general circulation model. *Geophysical Research Letters*, *15*(2), 1325–1328. https://doi.org/10.1029/GL015i012p01325

Siskind, D. E., Barth, C. A., & Roble, R. G. (1989). The response of thermospheric nitric oxide to an auroral storm: 1. Low and middle latitudes. *Journal of Geophysical Research*, *94*(A12), 16885–16898. https://doi.org/10.1029/JA094iA12p16885

Solomon, S. C., Burns, A. G., Emery, B. A., Mlynczak, M. G., Qian, L., Wang, W., et al. (2012). Modeling studies of the impact of high-speed streams and co-rotating interaction regions on the thermosphere-ionosphere. *Journal of Geophysical Research*, *117*(A9), A00L11. https://doi.org/10.1029/2011JA017417

Sutton, E. K. (2018). A new method of physics-based data assimilation for the quiet and disturbed thermosphere. *Space Weather*, *16*(6), 736–753. https://doi.org/10.1002/2017sw001785

Thayer, J., Liu, X., Lei, J., Pilinski, M., & Burns, A. (2012). The impact of helium on thermosphere mass density response to geomagnetic activity during the recent solar minimum. *Journal of Geophysical Research*, *117*(A7), A07315. https://doi.org/10.1029/2012JA017832

Zesta, E., & Oliveira, D. M. (2019). Thermospheric heating and cooling times during geomagnetic storms, including extreme events. *Geophysical Research Letters*, *46*(22), 12739–12746. https://doi.org/10.1029/2019GL085120

Zhang, Y., Paxton, L. J., Morrison, D., Marsh, D., & Kil, H. (2014). Storm-time behaviors of O/N_2 and NO variations. *Journal of Atmospheric and Solar-Terrestrial Physics*, *114*, 42–49. https://doi.org/10.1016/j.jastp.2014.04.003